Neuron
Article

Age-Related Homeostatic Midchannel Proteolysis of Neuronal L-type Voltage-Gated Ca^{2+} Channels

Ioannis E. Michailidis,[1] Kathryn Abele-Henckels,[1] Wei K. Zhang,[1] Bochao Lin,[1] Yong Yu,[1] Lawrence S. Geyman,[1] Michael D. Ehlers,[2] Eftychios A. Pnevmatikakis,[3] and Jian Yang[1,4,*]
[1]Department of Biological Sciences, Columbia University, New York, NY 10027, USA
[2]Neuroscience Research Unit, Pfizer Worldwide Research and Development, Cambridge, MA 02139, USA
[3]Department of Statistics, Columbia University, New York, NY 10027, USA
[4]Ion Channel Research and Drug Development Center, Kunming Institute of Zoology, Chinese Academy of Sciences, Kunming 650223, Yunnan, China
*Correspondence: jy160@columbia.edu
http://dx.doi.org/10.1016/j.neuron.2014.04.017

SUMMARY

Neural circuitry and brain activity depend critically on proper function of voltage-gated calcium channels (VGCCs), whose activity must be tightly controlled. We show that the main body of the pore-forming α_1 subunit of neuronal L-type VGCCs, $Ca_v1.2$, is proteolytically cleaved, resulting in $Ca_v1.2$ fragment channels that separate but remain on the plasma membrane. This "midchannel" proteolysis is regulated by channel activity, involves the Ca^{2+}-dependent protease calpain and the ubiquitin-proteasome system, and causes attenuation and biophysical alterations of VGCC currents. Recombinant $Ca_v1.2$ fragment channels mimicking the products of midchannel proteolysis do not form active channels on their own but, when properly paired, produce currents with distinct biophysical properties. Midchannel proteolysis increases dramatically with age and can be attenuated with an L-type VGCC blocker in vivo. Midchannel proteolysis represents a novel form of homeostatic negative-feedback processing of VGCCs that could profoundly affect neuronal excitability, neurotransmission, neuroprotection, and calcium signaling in physiological and disease states.

INTRODUCTION

Voltage-gated calcium channels (VGCCs; L, N, P/Q, R, and T types) control a plethora of physiological processes, from muscle contraction, heartbeat, neural communication, and hormone secretion to cell differentiation, motility, growth, and apoptosis (Catterall, 2000). Their mutations and dysfunction are linked to diverse disorders, such as epilepsy, migraine, ataxia, hypertension, arrhythmia, and autism (Cain and Snutch, 2011; Liao and Soong, 2010; Pietrobon, 2010; Striessnig et al., 2010; Zamponi et al., 2010). In neurons, L-type VGCCs regulate membrane excitability, Ca^{2+} signaling, and gene transcription (Catterall, 2000; Deisseroth et al., 2003; Dolmetsch, 2003; Wheeler et al., 2012). Changes in L-type VGCC activity are linked to aging and age-related neurodegenerative diseases (Moyer et al., 1992; Thibault and Landfield, 1996; Thibault et al., 1998), and variations in L-type VGCC genes are linked to neuropsychiatric diseases including schizophrenia, bipolar disorder, autism spectrum disorder, major depressive disorder, and attention deficit-hyperactivity disorder (Smoller et al., 2013).

To serve their vital and varying roles, VGCCs are subject to tight regulation by diverse pathways and mechanisms (Catterall, 2000; Zamponi and Currie, 2013). One form of regulation is proteolytic processing of the cytosolic C terminus (Ct) of the α_1 subunit ($Ca_v\alpha_1$) of L-type VGCCs (Brawley and Hosey, 1992; De Jongh et al., 1991, 1994; Gao et al., 2001; Gerhardstein et al., 2000; Hell et al., 1993; Hulme et al., 2005, 2006; Lai et al., 1990). This proteolysis produces a 30–45 kDa distal C-terminal fragment, which acts as an autoinhibitory domain (Hulme et al., 2006). Relief of this autoinhibition is believed to underlie the sympathetic nerve stimulation-induced increase of cardiac and skeletal muscle calcium currents, part of the "fight or flight" response (Fuller et al., 2010). In addition to this Ct fragment, a spectrum of other fragments has been observed in western blots of L-, N-, and P/Q-type $Ca_v\alpha_1$ (Kordasiewicz et al., 2006; Leenders et al., 2002, 2008; Ramakrishnan et al., 2006; Sakurai et al., 1995; Schiff et al., 2000; Scott et al., 1998; Westenbroek et al., 1995; Woppmann et al., 1994); the most consistent and prominent include 90 kDa, 150 kDa, and 170 kDa fragments. These fragments have generally been thought to be nonspecific degradation products. Intriguingly, however, short isoforms of L- and P/Q-type $Ca_v\alpha_1$ have been found in neurons and muscle cells (Malouf et al., 1992; Okagaki et al., 2001; Scott et al., 1998). Moreover, truncated P/Q-type $Ca_v\alpha_1$, generated by disease-causing mutations, are present in neurons (Jeng et al., 2008; Mezghrani et al., 2008; Page et al., 2004; Pietrobon, 2010; Scott et al., 1998; Wappl et al., 2002).

VGCCs are typically composed of a pore-forming $Ca_v\alpha_1$ and auxiliary $\alpha_2\delta$ and β ($Ca_v\beta$) subunits. Full-length $Ca_v\alpha_1$ is a large protein (with a predicted molecular mass of 190–280 kDa) consisting of four homologous repeats, each containing six transmembrane segments; the four repeats are connected by cytoplasmic loops termed the I-II loop, II-III loop, and III-IV loop. The aforementioned findings motivated us to investigate

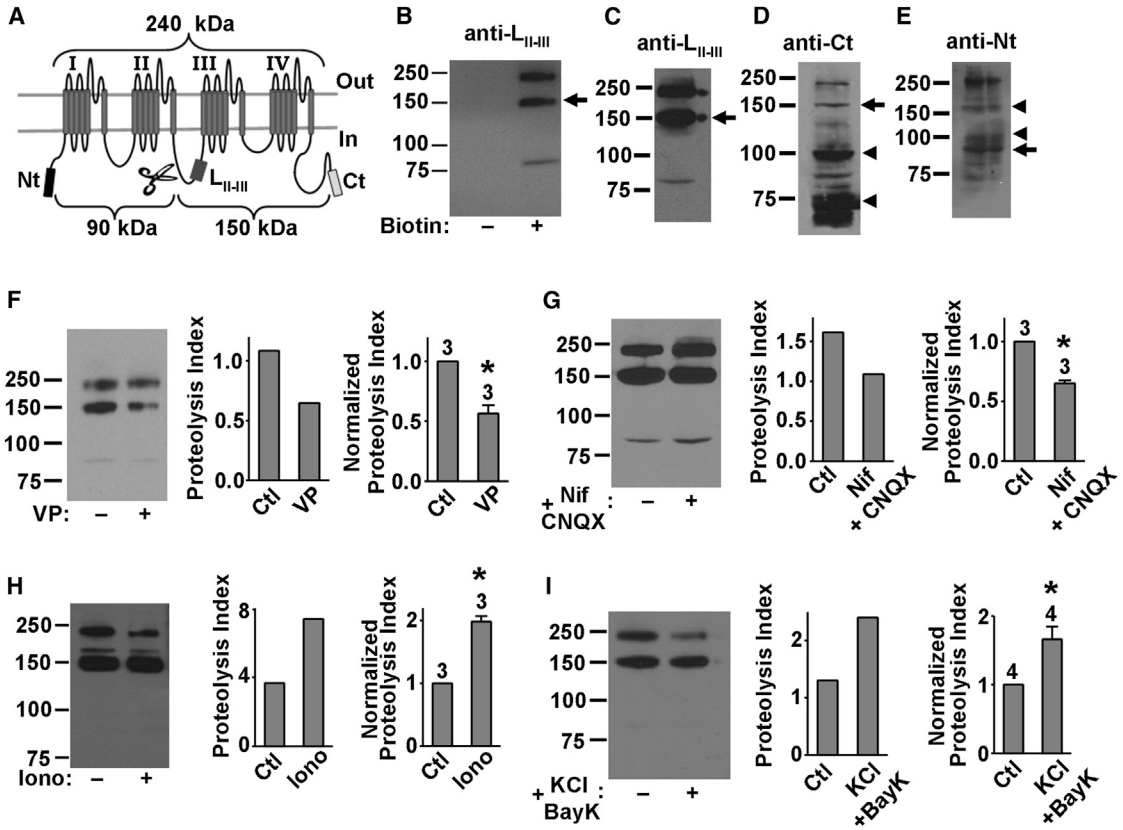

Figure 1. Midchannel Proteolysis of Native $Ca_v1.2$ in Cortical Neurons and Its Dependence on Channel Activity

(A) Domain topology of $Ca_v1.2$. Indicated are epitope locations for three antibodies (anti-L_{II-III}, anti-Ct, and anti-Nt) and predicted molecular masses for full-length $Ca_v1.2$ and two fragment channels generated by a presumed proteolytic cut (scissors).

(B) Western blot with anti-L_{II-III} of native $Ca_v1.2$ in surface-biotinylated (+) and nonbiotinylated (–) cortical slices from 6-week-old rats, showing a 150 kDa band (arrow).

(C–E) Western blot with anti-L_{II-III} (C), anti-Ct (D), or anti-Nt (E) of native $Ca_v1.2$ from the same sample of surface-biotinylated cortical slices.

(F–I) Channel-activity-dependent regulation of midchannel proteolysis. (F) Verapamil (VP; 65 μM, 2 hr); (G) nifedipine (Nif; 10 μM, 2 hr) and CNQX (21.5 μM, 2 hr); (H) ionomycin (Iono; 3 μM, 45 min); (I) BayK8644 (14 μM, 40 min) and 65 mM KCl (40 min). Left: representative western blot with anti-L_{II-III} of $Ca_v1.2$ in cortical slices treated with either vehicle (control; Ctl) or the indicated reagent(s) before surface biotinylation. Middle: bar graph depicting the proteolysis index (intensity ratio of the 150 kDa/240 kDa band) for the representative gel. Right: summary graph showing data pooled from the indicated number of independent experiments. In this and all subsequent figures, data are represented as mean ± SEM, and single and double asterisks denote statistical differences. $p < 0.01$ by t test.

See also Figure S5.

the existence and functional importance of proteolytic cleavage in the core (i.e., the four repeats and the tethering cytosolic loops) of $Ca_v\alpha_1$. We find that indeed the core of native brain L-type $Ca_v\alpha_1$, $Ca_v1.2$, undergoes extensive regulated proteolysis, generating $Ca_v1.2$ fragments on the plasma membrane and greatly influencing channel activity. We further find that this proteolysis is age dependent and can be reversed in vivo by reducing L-type channel activity. To distinguish this proteolytic event from C-terminal proteolysis, we refer to it as "midchannel proteolysis."

RESULTS

Biochemical Detection of Midchannel Proteolysis of Native L-type Channels

We first studied midchannel proteolysis of native L-type channels in cortical brain slices freshly isolated from 6-week-old rats. Surface channels were biotinylated and analyzed by western blot. When probed with an antibody against the $Ca_v1.2$ II-III loop (anti-L_{II-III}; epitope T821–S838 of rat brain $Ca_v1.2$; Figure 1A), two prominent bands were routinely observed: 240 kDa (full-length $Ca_v1.2$) and 150 kDa (Figures 1B–1I). An 85 kDa band was also sometimes detected (Figures 1B–1G). The 150 kDa band was also recognized (Figure 1D, arrow) by an antibody against the distal C terminus (anti-Ct; epitope G2127–L2143; Figure 1A). Thus, this fragment appears to contain part of the II-III loop, repeats III and IV, and the C terminus (Figure 1A). Anti-Ct also labeled bands at 100 kDa and 70 kDa (Figure 1D, arrowheads). Probing with an antibody against the N terminus (anti-Nt; epitope V2–N14; Figure 1A) also revealed several low molecular weight (MW) bands, including those at 175 kDa, 100 kDa, and 90 kDa (Figure 1E, arrowheads and arrow). These results suggest that native $Ca_v1.2$ in cortical neurons undergo extensive proteolysis in vivo

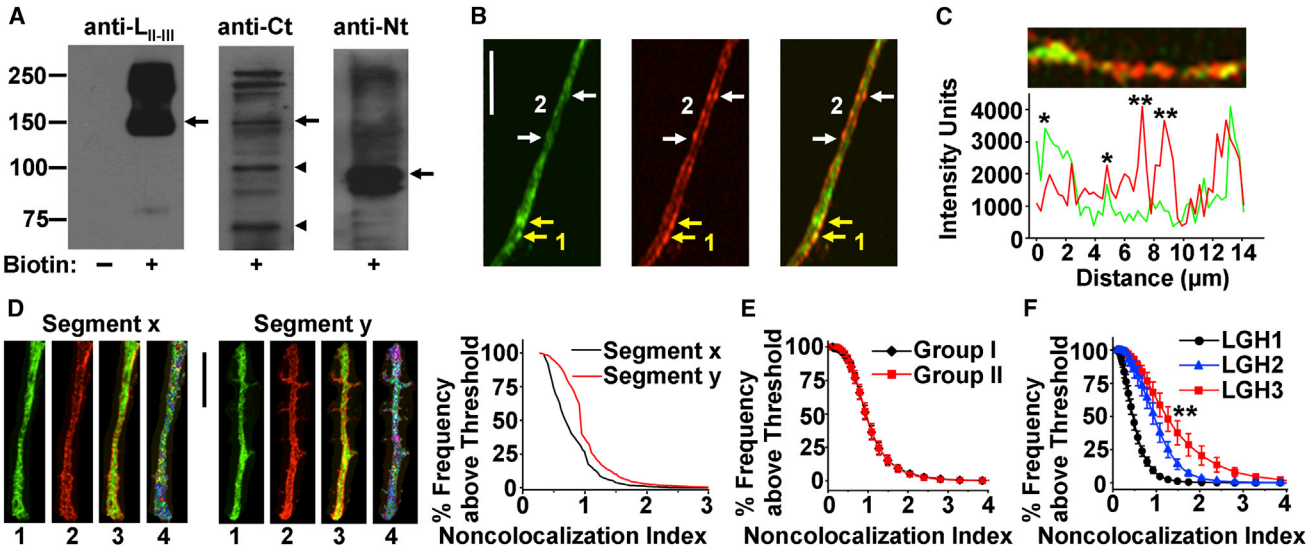

Figure 2. Visualization of Midchannel Proteolysis of $Ca_v1.2$ in the Plasma Membrane of Cultured Hippocampal Neurons

(A) Western blot with the indicated antibodies of native $Ca_v1.2$ from the same preparation of surface-biotinylated neurons.

(B) Confocal images of a representative dendritic segment of a neuron expressing LGH3. Left: surface and intracellular LGH3 indicated by GFP. Middle: surface LGH3 indicated by anti-HA+Alexa 594 secondary antibodies. Right: overlay. Exemplar clusters of red/green colocalization and noncolocalization are marked by yellow and white arrows, respectively. The scale bar represents 5 μm.

(C) Fluorescence intensity profile (bottom) of another dendritic segment (top). Exemplar clusters of red/green colocalization and noncolocalization are marked by * and **, respectively.

(D) Quantification of red/green colocalization in two dendritic segments displaying visually different extents of midchannel proteolysis. Left and middle: images of GFP (lane 1), HA-Alexa 594 (lane 2), overlay (lane 3), and the voxels selected according to our analysis protocol (lane 4). Right: cumulative distribution of the NCI for the two selected dendritic segments. The scale bar represents 10 μm.

(E) Ensemble cumulative distribution of the NCI from the dendrites of neurons expressing LGH3 randomly divided into two groups (n = 15 each, same culture).

(F) Ensemble cumulative distribution of the NCI from the dendrites of neurons expressing LGH1 (n = 23), LGH2 (n = 15), and LGH3 (n = 13). All experiments were performed in parallel. The three distributions were significantly different. $p < 0.01$ by t test.

See also Figures S1 and S2.

and that the cleaved products reside in the plasma membrane as fragment channels. The 150 kDa fragment detected by both anti-L_{II-III} and anti-Ct (Figures 1C and 1D, arrows) and the 90 kDa fragment detected by anti-Nt (Figure 1E, arrow) are complementary, adding up to 240 kDa (expected full-length $Ca_v1.2$ MW). As the 150 kDa fragment was the most robust, we focused subsequent studies on this fragment.

Midchannel Proteolysis Is Bidirectionally Regulated

We next investigated whether $Ca_v1.2$ midchannel proteolysis is a regulated event occurring in vivo. To minimize nonspecific degradation, abundant protease inhibitors were added and all procedures were performed rapidly at 4°C. More critically, as nonspecific degradation is an unregulated event, we investigated whether midchannel proteolysis could instead be disrupted or enhanced. Agents that affect intracellular Ca^{2+}, L-type channel activity, and/or cell excitability were used to treat cortical slices prior to surface biotinylation. To quantify midchannel proteolysis, densitometry was used to define a proteolysis index as the intensity ratio of the 150 kDa/240 kDa bands detected by anti-L_{II-III}. This index is unaffected by the total protein amount since it is the ratio of two bands from the same lane/sample. The nonnormalized proteolysis index differed among preparations (Figures 1F–1I), reflecting intrinsic animal-to-animal variation. However, this variation does not affect pairwise comparison of control and test results, which were obtained from parallel experiments from the same animal.

Midchannel proteolysis was decreased by the L-type channel antagonist verapamil (Figure 1F) or by an activity-suppressing cocktail of nifedipine (another L-type channel antagonist) and the glutamate receptor inhibitor 6-cyano-7-nitroquinoxaline-2,3-dione (CNQX) (Figure 1G). In contrast, midchannel proteolysis was increased by the Ca^{2+} ionophore ionomycin (Figure 1H) and by an activity-enhancing cocktail of high extracellular K^+ and L-type channel agonist BayK8644 (Figure 1I). Thus, midchannel proteolysis correlated with L-type channel activity and intracellular Ca^{2+} levels. This *bidirectional* regulation suggests that $Ca_v1.2$ midchannel proteolysis takes place in vivo.

Regulated midchannel proteolysis of native $Ca_v1.2$ was also observed in cultured hippocampal neurons (Figure 2A; Figure S1A available online). After surface biotinylation and western blot, anti-L_{II-III} robustly detected bands at 240 kDa and 150 kDa (Figure 2A, left, arrow). Both bands were also detected by anti-Ct (Figure 2A, middle, arrow), as were a 100 kDa band and a 70 kDa band (arrowheads), which were also present in cortical slices (Figure 1D, arrowheads). In the same samples, anti-Nt visualized the 240 kDa band and a 90 kDa band (Figure 2A, right, arrow). The detection of the complementary 150 kDa and 90 kDa bands

in both cortical slices and cultured hippocampal neurons is consistent with proteolysis in the II-III loop of $Ca_v1.2$.

Visualization of Midchannel Proteolysis Reveals Separation of Cleaved Fragment Channels

The above biochemical results indicate that the complementary 150 kDa and 90 kDa $Ca_v1.2$ fragments are present on the plasma membrane. Do these cleaved fragments remain associated on the cell surface? To address this question, we transfected cultured hippocampal neurons with LGH3, a $Ca_v1.2$ tagged with GFP on the N terminus and hemagglutinin epitope tag (HA) on an extracellular loop of repeat III (Figure S1B), and visualized the channels by confocal microscopy. LGH3 generated currents in *Xenopus* oocytes (Figure S1C) and expressed robustly in cultured hippocampal neurons (Figure S2). Labeling the HA tag with an anti-HA antibody and Alexa 594 under non-permeabilizing conditions revealed LGH3 on the plasma membrane (Figure S2A, red). $Ca_v1.2$ with GFP but without the HA tag (LGN) showed no surface labeling (Figure S2B), indicating that the anti-HA labeling was specific.

In optical sections, Alexa 594-labeled dendrites of LGH3-expressing neurons often displayed a membrane-associated pattern (Figure 2B, middle), consistent with red labeling representing surface $Ca_v1.2$. Surface $Ca_v1.2$ channels tend to form clusters (Figures 2B and 2C), as has been reported (Di Biase et al., 2011). Intriguingly, in some locations, green and red clustered separately (Figure 2B, left and Figure 2C). Green-only clusters likely represent intracellular LGH3 and are expected, but red-only clusters are anomalous—in theory, GFP and HA signals should colocalize since the two tags are on the same protein. The separation of red and green, however, is consistent with cleavage of $Ca_v1.2$ somewhere between the two tags. Furthermore, it suggests that the cleavage products on the plasma membrane dissociate from one another.

We developed an unbiased procedure to quantify red/green separation in imaging experiments: (1) a software routine scanned optical sections of dendrites and automatically detected red "voxels," each with a dimension of 0.211 × 0.211 × 0.211 μm (typical dendrites are <2 μm in diameter), and ~10,000 voxels were typically found per neuron; (2) the intensity of red and green for each voxel was measured; and (3) the red/green ratio, termed the noncolocalization index (NCI), was calculated, binned, and graphed in a cumulative frequency (ordinate) versus NCI (abscissa) plot (Figures 2D–2F).

Three conclusions apply to the results of this analysis protocol: (1) voxels of high NCI are likely proteolysis hot spots and contain proteolytically cleaved, HA-containing fragment channels, including the 150 kDa fragment; (2) the higher the NCI, the more extensive the proteolysis; and (3) a shift of the distribution curve to the right signifies greater proteolysis.

The above analysis protocol was calibrated in two dendritic segments selected for their different extent of red/green separation (Figure 2D). As expected, the segment displaying a higher number of visual red-only spots (segment y) showed a right-shifted NCI distribution (Figure 2D). In another critical test, LGH3-expressing neurons from the same culture randomly divided into two groups showed identical ensemble NCI distributions (Figure 2E), strongly validating the analysis protocol.

Visualization of Midchannel Proteolysis Suggests Multiple Cleavage Sites

If red/green separation represents midchannel proteolysis of $Ca_v1.2$, it should decrease when GFP and HA are closer together on the channel. Moreover, the appearance of multiple $Ca_v1.2$ fragments in western blots (Figures 1D, 1E, and 2A) suggests that there may be more than one cleavage site in the $Ca_v1.2$ core domain. To test these predictions, we constructed two additional GFP/HA double-tagged $Ca_v1.2$ subunits named LGH1 and LGH2 (HA positioned extracellularly on repeat I or II, respectively). LGH1 and LGH2 produced currents in oocytes (Figure S1C), confirming they traffic to the plasma membrane and are functional. Parallel imaging experiments showed markedly reduced red/green separation as the two tags were moved closer together (Figure 2F). These results further validate the analysis protocol and support the notion that red/green separation is indicative of midchannel proteolysis. They also suggest proteolysis not only in the II-III loop but also in the I-II loop.

Molecular Determinants of Midchannel Proteolysis

To examine the signaling pathways of midchannel proteolysis, we first tested the role of calpain, a Ca^{2+}-sensitive protease likely responsible for the cleavage of the $Ca_v1.2$ C terminus (Hell et al., 1996; Hulme et al., 2006). A cocktail of calpain inhibitors significantly reduced midchannel proteolysis in hippocampal neurons, detected by both western blot and imaging (Figures 3A and 3B), supporting calpain's involvement. However, residual midchannel proteolysis persisted (Figure 3A), suggesting additional proteases. We thus tested the role of the ubiquitin-proteasome system, a common route for protein degradation. The midchannel proteolysis of LGH3 was markedly reduced by a cocktail of ubiquitin aldehyde, a general inhibitor of ubiquitination, and MG-132, a proteasome inhibitor (Figure 3C), and by mutating a putative ubiquitination motif on LGH3 (Figure 3D). Two PEST ([proline, glutamic acid, serine, and threonine]-rich) sequences have been found in $Ca_v1.2$, in the I-II and II-III loops (Catalucci et al., 2009) (named PEST1 and PEST3, respectively; Figure 3E); PEST sequences serve as signals for rapid proteolysis and possible degradation by the ubiquitin-proteasome system in various proteins (Rechsteiner and Rogers, 1996). Midchannel proteolysis was greatly reduced by PEST3 deletion (Figure 3F) and was virtually abolished by PEST1 deletion (Figure 3G; Figure S3C). These results identify structural elements regulating midchannel proteolysis and suggest a compelling role for the ubiquitin-proteasome system.

Separation of Fragment channels Is Regulated by Channel Activity

Midchannel proteolysis of LGH3, like that of endogenous $Ca_v1.2$, was regulated by L-type channel activity. Depolarizing neurons with high extracellular K^+, in the absence or presence of BayK8644, increased midchannel proteolysis in both imaging and western blot experiments (Figures 4A and 4B). On the other hand, treatment with nifedipine, even in the presence of high extracellular K^+, decreased it (Figures 4C and 4D; Figure S4). These results further support the notion that the red/green separation is a consequence and manifestation of midchannel proteolysis.

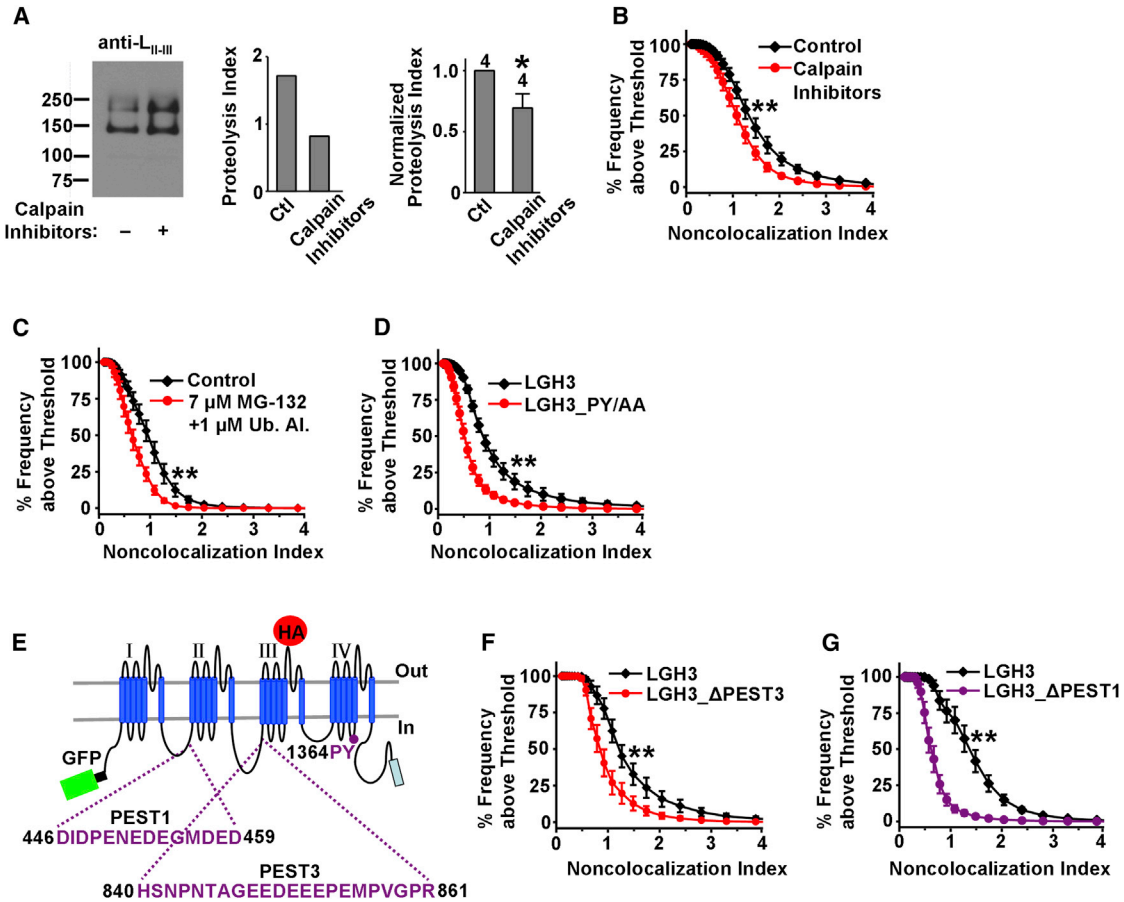

Figure 3. Signaling Pathways and Molecular Determinants of $Ca_V1.2$ Midchannel Proteolysis

(A) Role of calpain. Left: representative western blot with anti-L_{II-III} in hippocampal neurons treated, before surface biotinylation, with a cocktail of calpain inhibitors (200 nM calpeptin, 1 μM N-acetyl-Leu-Leu-Norleu-al, and 270 nM calpain inhibitor III) for 80 min at 37°C. Middle: proteolysis index for the representative gel. Right: summary graph showing data pooled from four independent experiments. $p < 0.05$ by t test.

(B) Ensemble cumulative distribution of the NCI from the dendrites of neurons expressing LGH3 treated with DMSO (control; n = 24) or calpain inhibitors (n = 19). $p < 0.05$ by t test.

(C) Ensemble cumulative distribution of the NCI from the dendrites of neurons expressing LGH3 (n = 13) treated with DMSO (control) or a cocktail of MG-132 (7 μM) and ubiquitin aldehyde (1 μM) for 75 min at 37°C. $p < 0.05$ by t test.

(D) Ensemble cumulative distribution of the NCI from the dendrites of neurons expressing LGH3 (n = 16) or LGH3_PY/AA (n = 17), where residues P1364 and Y1365 of LGH3 were mutated to alanine. $p < 0.01$ by t test.

(E) Schematic domain topology of LGH3, marking the positions and amino acid sequences of the PEST1 site, PEST3 site, and PY motif.

(F) Ensemble cumulative distribution of the NCI from the dendrites of neurons expressing LGH3 (n = 19) or LGH3_ΔPEST3 (n = 17), where residues H840–R861 of LGH3 were deleted. $p < 0.05$ by t test.

(G) Ensemble cumulative distribution of the NCI from the dendrites of neurons expressing LGH3 (n = 19) or LGH3_ΔPEST1 (n = 15), where residues D446–D459 of LGH3 were deleted. Representative dendrites are shown in Figure S3C. $p < 0.01$ by t test.

In (B)–(D), (F), and (G), all experiments in each panel were performed in parallel. See also Figure S3.

Functional Impact of Midchannel Proteolysis

We next investigated the functional effect of midchannel proteolysis on calcium channel currents in several ways. First, we tested the long-term effect of two treatments shown to differentially alter midchannel proteolysis on native VGCC currents in hippocampal neurons. Incubating neurons with high K^+ and BayK8644 (followed by washout) increased midchannel proteolysis (Figures 4A and 4B) and *reduced* VGCC currents (Figure 4E), whereas incubation with nifedipine (followed by washout) decreased midchannel proteolysis (Figures 4C and 4D) and *enhanced* VGCC currents (Figure 4F). These results are consistent with a hypothesis that midchannel proteolysis serves to homeostatically regulate VGCC activity, keeping at bay excessive Ca^{2+} influx that could have a potential deleterious effect on neurons.

Second, in another test of the long-term effect of midchannel proteolysis, we inserted a cleavage motif for the tobacco etch virus protease (TEVp) in the II-III loop of LGH3 (between D815 and G816, upstream of the anti-L_{II-III} epitope T821–S838), generating LGH3_TEVp (Figure 5A). *Xenopus* oocytes expressing

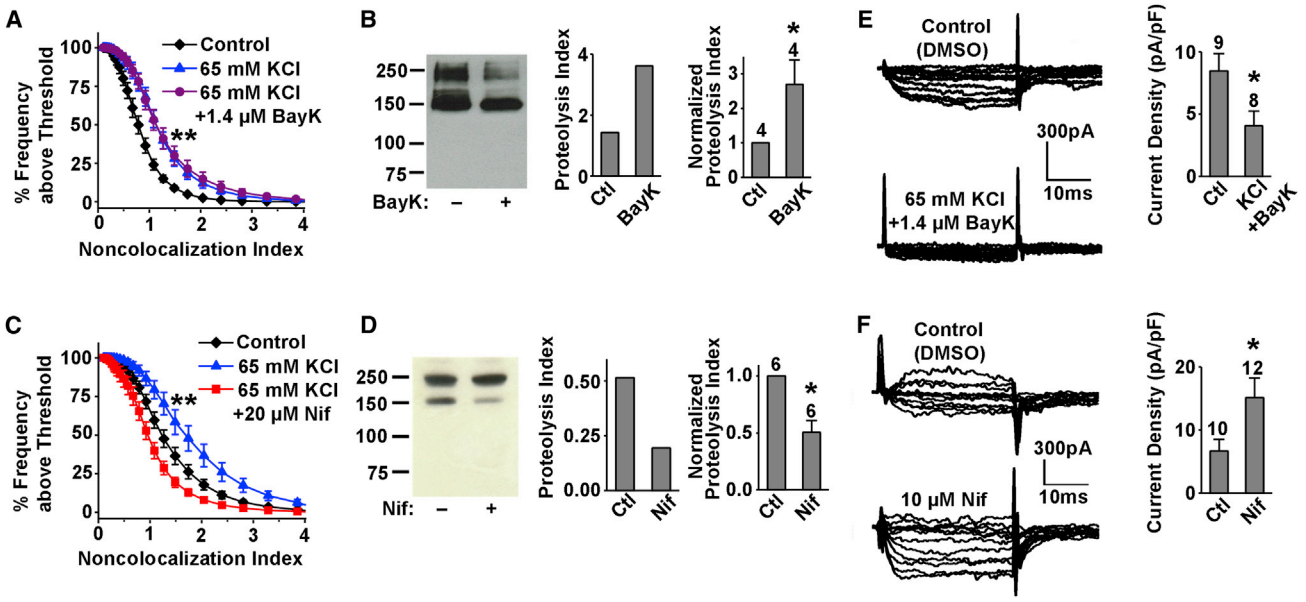

Figure 4. Channel-Activity-Dependent Regulation of $Ca_v1.2$ Midchannel Proteolysis and Ca^{2+} Channel Currents in Cultured Hippocampal Neurons

(A and C) Ensemble cumulative distribution of the NCI from the dendrites of neurons expressing LGH3. Neurons were treated for 30 min with DMSO (control), DMSO and 65 mM KCl, or 1.4 μM BayK8644 and 65 mM KCl (n = 13 for all) in (A), or with DMSO (control) (n = 19), DMSO and 65 mM KCl (n = 14), or 20 μM nifedipine and 65 mM KCl (n = 18) in (C). Representative dendrites are shown in Figure S4A. All experiments in each panel were performed in parallel. In (A), the two treated groups were significantly different from the control ($p < 0.01$ by t test) but not from each other; in (C), all three distributions were significantly different ($p < 0.01$ by t test). The same results were obtained from two other independent cultures.

(B and D) Channel-activity-dependent regulation of midchannel proteolysis. Left: representative western blot with anti-L_{II-III} in neurons treated (1 hr) with DMSO (Ctl) or BayK8644 (1.4 μM) (B) or nifedipine (10 μM) (D) before surface biotinylation. Middle: proteolysis index for the representative gel. Right: summary graph showing data pooled from the indicated number of independent experiments. $p < 0.01$ by t test.

(E and F) Whole-cell Ca^{2+} channel currents from neurons blindly treated for 30 min with DMSO (Ctl), 65 mM KCl and 1.4 μM BayK8644 (E), or 10 μM nifedipine (F). Left: representative family of currents recorded from the indicated neuron. Right: summary graph of the maximal current density for the indicated group of neurons. The number of blind recordings is indicated above the bar. $p < 0.05$ by t test.

See also Figure S4.

LGH3, LGH3_TEVp, or LGH3 with TEVp had comparable currents (Figure 5B, top), but those expressing LGH3_TEVp with TEVp had much smaller currents (Figure 5B, top). The latter group showed a prominent 150 kDa fragment detected by anti-L_{II-III} on the plasma membrane, with a drastic concomitant reduction of the 270 kDa ($Ca_v1.2$+27 kDa GFP) full-length band (Figure 5B, bottom). This 150 kDa fragment, largely absent in the three control groups, most likely represents the C-terminal product of specific TEVp cleavage of LGH3_TEVp. The decreased current of LGH3_TEVp by TEVp proteolysis validates the hypothesis that midchannel proteolysis downregulates VGCC currents.

Third, we examined the acute effect of midchannel proteolysis. To accomplish this, we engineered TEVp cleavage sites in the I-II and II-III loops of $Ca_v2.1$ (this mutant is called $Ca_v2.1$_TEVp), and tested the effect of purified recombinant TEVp on $Ca_v2.1$_TEVp channels in inside-out membrane macropatches excised from *Xenopus* oocytes. $Ca_v2.1$ was chosen because its currents run down much more slowly than $Ca_v1.2$ currents do. A 2 min application of TEVp did not abolish channel activity, but did produce an irreversible left shift of the activation curve of $Ca_v2.1$_TEVp but not WT $Ca_v2.1$ channels (Figure 5C, bottom). A catalytically inactive TEVp (carrying the C151A mutation) had no effect (Figure 5C, bottom). These results indicate that midchannel proteolysis alters VGCC gating, leaving a biophysical imprint.

Fourth, we constructed three pairs of complementary $Ca_v1.2$ fragment channels, mimicking midchannel proteolysis in loop I-II, II-III, or III-IV (Figure 6A), and tested their activity in oocytes by two-electrode voltage clamp. None of the six recombinant fragment channels, named A1, A2, B1, B2, C1, and C2, produced currents when individually expressed in oocytes (Figure 6B). However, all three complementary pairs produced sizeable currents, albeit their amplitude was smaller than that of $Ca_v1.2$ currents (Figure 6C). Channels formed by all three complementary pairs displayed a right-shifted current-voltage (I-V) curve (Figure 6D) and a change in the voltage dependence of inactivation (Figure 6E). Thus, although individual fragment channels do not conduct current, when properly paired they can assemble and reach the plasma membrane to form functional channels with distinct biophysical properties. We also examined expression of four noncomplementary fragment pairs, A1+C2, A2+B1, A2+C1, and B2+C1, in oocytes. The first three pairs did not produce any currents, while the last pair produced

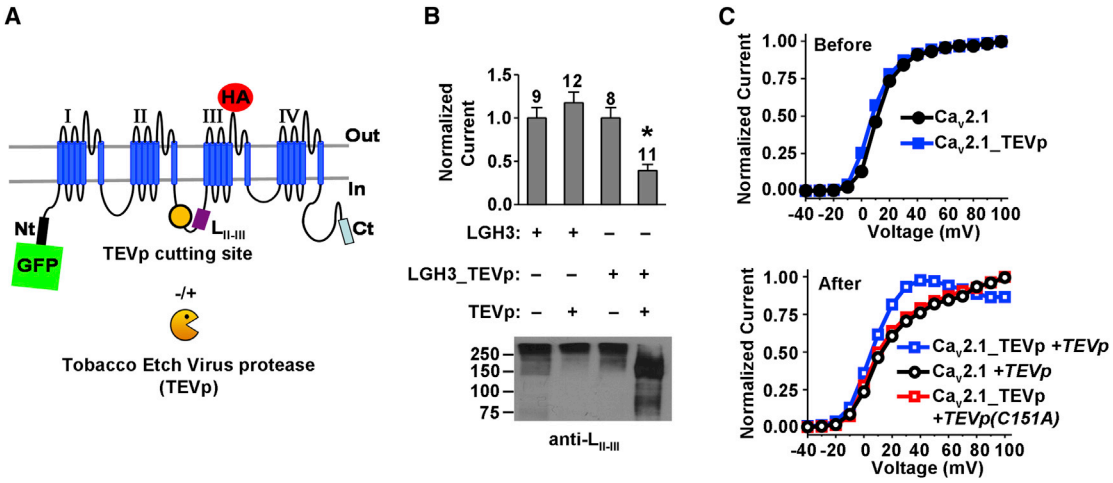

Figure 5. Functional Effect of Midchannel Cleavage at an Engineered Site on Ca^{2+} Channel Currents and Properties

(A) Schematic of LGH3_TEVp, which contains a TEVp cutting site (yellow circle) in the II-III loop between D815 and G816, upstream of the anti-L_{II-III} epitope T821–S838.

(B) Whole-cell currents (top) recorded at −10 mV from oocytes expressing the indicated constructs (middle). Currents were normalized to the mean value of the leftmost control group. The number of measurements is indicated above the bars. $p < 0.01$ by t test. Bottom: western blot with anti-L_{II-III} of surface-biotinylated oocytes from the exact same groups.

(C) Voltage dependence of activation of currents recorded from inside-out macropatches excised from oocytes expressing $Ca_v2.1$_TEVp or WT $Ca_v2.1$, before (top) or after (bottom) bath application of 100 μM purified TEVp or TEVp(C151A). Standard error is smaller than the symbols (n = 7–10).

See also Figure S6A.

a small current (Figure S6B). These results suggest that all four repeats of $Ca_v\alpha_1$ are needed to form functional channels and that certain noncomplementary $Ca_v\alpha_1$ fragments containing, altogether, more than four repeats may still assemble and form functional channels, albeit poorly.

Lastly, we examined whether the recombinant fragment channels change the properties of full-length $Ca_v1.2$. Previous studies have shown that coexpression of $Ca_v\alpha_1$ fragments with full-length $Ca_v\alpha_1$ often suppresses WT channel currents in a dominant-negative manner and sometimes alters their biophysical properties (Ebihara et al., 2002; Jeng et al., 2008; Mezghrani et al., 2008; Page et al., 2004, 2010; Raghib et al., 2001; Raike et al., 2007). We found that fragment C2 greatly dampened $Ca_v1.2$ current amplitude, while other fragments did not have a significant dominant-negative effect (Figure 6F). Fragments A1 and A2 shifted the $Ca_v1.2$ I-V curve to the right (Figure 6G) and increased $Ca_v1.2$ inactivation (Figure 6H). Fragments B1 and B2 did not have a significant effect (Figures 6I and 6J). Fragment C1 shifted $Ca_v1.2$'s I-V curve to the left (Figure 6K) and markedly increased $Ca_v1.2$ inactivation (Figure 6L). Thus, $Ca_v1.2$ fragment channels can have multifaceted effects on full-length $Ca_v1.2$ channels.

Midchannel Proteolysis Is Age Dependent and Can Be Reversed In Vivo

Because changes in L-type Ca^{2+} channel activity have been linked to normal aging (Moyer et al., 1992; Thibault and Landfield, 1996; Thibault et al., 1998), we examined whether midchannel proteolysis of $Ca_v1.2$ is regulated across the lifespan. Cortical slices were freshly isolated, in strict parallel, from rats of four age groups (10 days, 6 weeks, 6 months, and 16 months), and cell-surface $Ca_v1.2$ was examined by western blot (Figure 7A). Midchannel proteolysis increased steadily and significantly with age, being approximately seven times more pronounced in 16-month-old rats than in 10-day-old rats (Figure 7A). Moreover, the elevated midchannel proteolysis in the 16-month-old rats could be partially reversed by a 3- to 5-week treatment with verapamil, an L-type VGCC blocker commonly used for hypertension, cardiac arrhythmia, cluster headache, and bipolar disorder (Figure 7B), at a dosage equivalent to that used for human patients, adjusted for body weight and metabolic rate.

DISCUSSION

We have uncovered a form of regulation of L-type VGCCs, namely, proteolytic cleavage of the main body of native $Ca_v1.2$ channels. Strikingly, cleaved fragment channels are present on the plasma membrane and can dissociate from each other. This midchannel proteolysis is not a result of nonspecific protein degradation, since it is bidirectionally regulated, inversely correlated with Ca^{2+} channel activity, and dependent on age. The finding that midchannel proteolysis in freshly isolated cortical slices and cultured hippocampal neurons can be reduced by inhibiting L-type Ca^{2+} channel activity (Figures 1F, 1G, 4C, and 4D) suggests that it is an ongoing physiological event occurring in native cells. This finding, together with the observation that midchannel proteolysis can be enhanced by increased intracellular Ca^{2+} (Figure 1H; Figure S1A) or increased L-type Ca^{2+} channel activity (Figures 1I, 4A, and 4B), suggests that midchannel proteolysis is a homeostatic/neuroprotective mechanism to regulate intracellular Ca^{2+}. The dramatic increase of $Ca_v1.2$

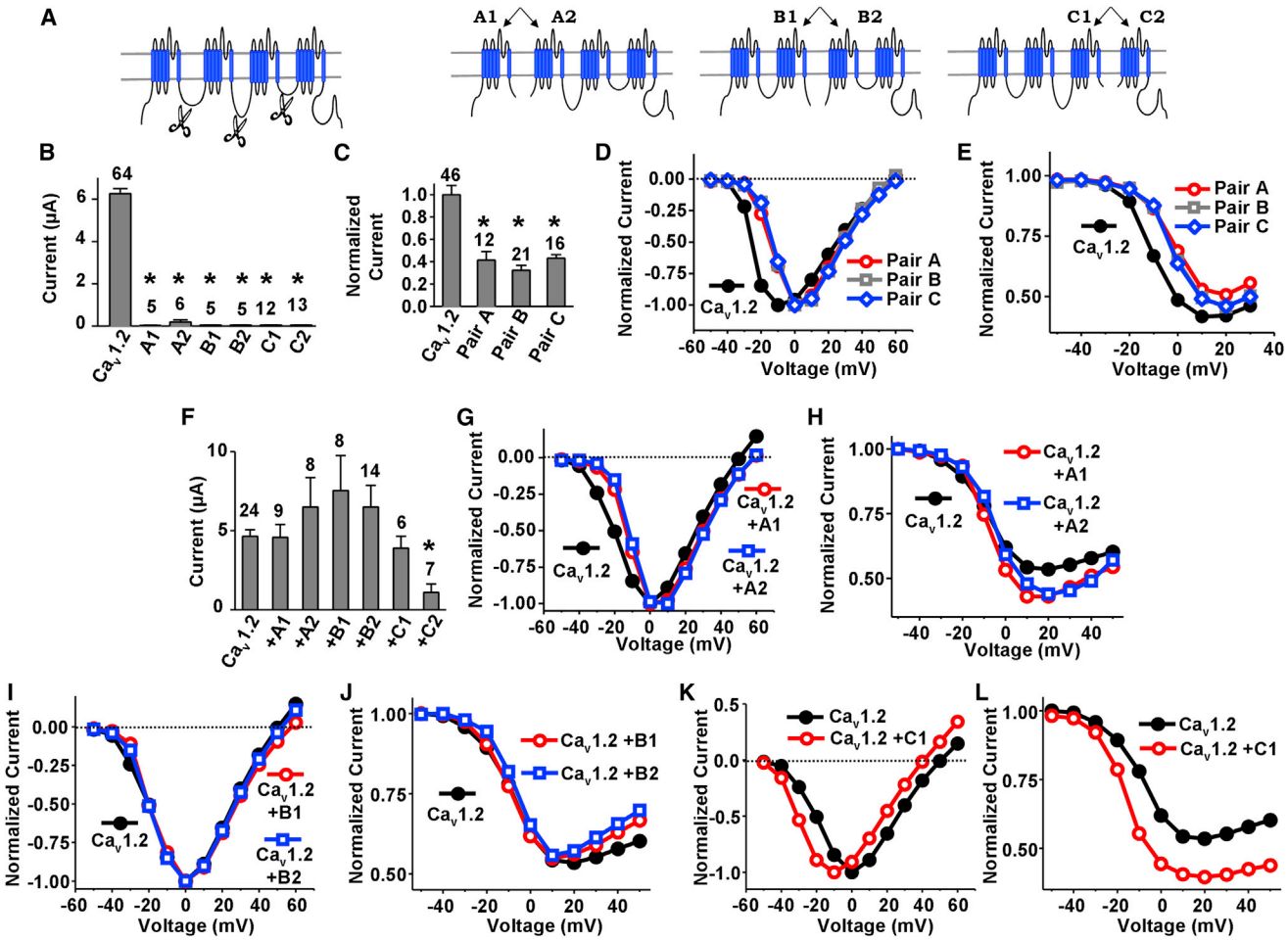

Figure 6. Functional Properties and Effects of Fragment Channels

(A) Schematic of three possible cuts (scissors) of $Ca_v1.2$ and three pairs of recombinant complementary fragment channels.

(B and C) Whole-cell currents recorded at −10 mV from oocytes expressing the indicated recombinant fragment channels (B) or proper pairs (C). $p < 0.01$ by t test.

(D and E) Current-voltage relationship (D) and voltage dependence of inactivation (E) of currents recorded from oocytes expressing the indicated constructs. Standard error is smaller than the symbols (n = 6–18).

(F) Whole-cell currents recorded at −10 mV from oocytes expressing full-length $Ca_v1.2$, with or without the indicated recombinant fragment channel coexpressed. $p < 0.01$ by t test.

(G–L) Current-voltage relationship (G, I, and K) and voltage dependence of inactivation (H, J, and L) of currents recorded from oocytes expressing the indicated $Ca_v1.2$ constructs. Standard error is smaller than the symbols (n = 3 for L and n = 6–14 for other panels). The effect of C2 could not be assessed because the whole-cell current in those experiments was too small to allow accurate measurements (see F, rightmost bar).

See also Figure S6B.

midchannel proteolysis with age in vivo is likely a manifestation of such a homeostatic/neuroprotective mechanism: as neurons age, their L-type Ca^{2+} channel currents increase (Moyer et al., 1992; Thibault and Landfield, 1996; Thibault et al., 1998), leading to increased intracellular Ca^{2+} and a compensatory increase of $Ca_v1.2$ midchannel proteolysis.

The conditions shown in this study that enhance $Ca_v1.2$ midchannel proteolysis, such as increased intracellular Ca^{2+}, increased Ca^{2+} channel activity, and increased age, did not change the levels of surface Na^+/K^+ ATPases and did not increase proteolysis of poly(ADP-ribose) polymerase (PARP) (Figure S5), an apoptotic protein marker whose proteolytic cleavage has been correlated with programmed cell death (Chaitanya et al., 2010), suggesting that midchannel proteolysis of $Ca_v1.2$ is not simply an early step of L-type VGCC degradation, not due to cell damage, and not a prelude to cell death. That midchannel proteolysis is robustly detected in freshly isolated cortical slices and hippocampal neurons (Figures 1, 2, 3, 4 and 7), bidirectionally regulated (Figures 1F–1I and 4A–4D), strongly linked to aging (Figure 7A), and reversible in animals by an L-type VGCC blocker (Figure 7B) suggests that midchannel proteolysis is a physiological mechanism of feedback regulation of L-type VGCCs in intact cells in vivo.

In our imaging experiments, we postulated that the red/green separation is indicative of midchannel proteolysis of $Ca_v1.2$, and that the lateral shifts of the ensemble NCI plots represent

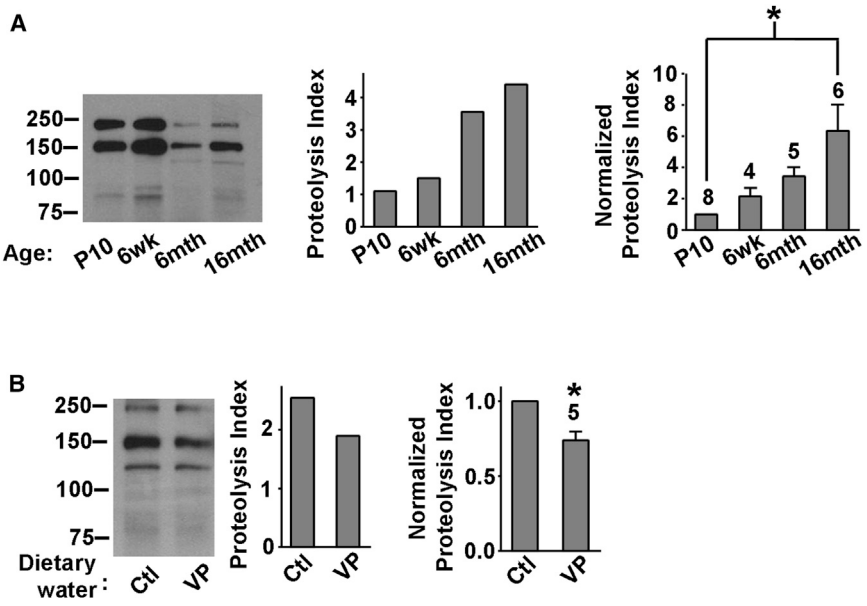

Figure 7. Midchannel Proteolysis Is Age Dependent and Can Be Reversed by an L-type VGCC Blocker In Vivo

(A) Progressive increase of midchannel proteolysis with age. Left: representative western blot with anti-$L_{II\text{-}III}$ of native $Ca_v1.2$ in surface-biotinylated rat cortical slices from the indicated age groups. Middle: proteolysis index for the representative gel. Right: summary graph showing data pooled from the indicated number of independent experiments. $p < 0.01$ by ANOVA. Each independent experiment consisted of parallel dissections of the age groups involved (see Experimental Procedures).

(B) Reduction of midchannel proteolysis by oral administration of verapamil. Left: representative western blot with anti-$L_{II\text{-}III}$ of native $Ca_v1.2$ in surface-biotinylated cortical slices from 16-month-old rats fed with water or water medicated with 12.5 mg/day of verapamil for 3–5 weeks. Middle: proteolysis index for the representative gel. Right: summary graph showing data pooled from five independent experiments. $p < 0.01$ by t test.

See also Figure S7.

changes in midchannel proteolysis. Is it possible, however, that such shifts are due to changes in the relative expression level of $Ca_v1.2$ in the plasma membrane versus intracellular compartments? To examine this possibility, we plotted the ratio of total red over total green (i.e., surface plus intracellular) fluorescence for four drug treatments that produced shifts in the NCI: calpain inhibitors, proteasome inhibitors, 65 mM KCl or 65 mM KCl+BayK8644, and 65 mM KCl or 65 mM KCl+nifedipine. The exact same neurons used for the NCI plots were used in the total fluorescence plots. In each case, the drug treatment did not significantly change total red/total green fluorescence compared to its untreated control group (Figures S3A, S3B, S4B, and S4C). This analysis is consistent with the notion that NCI shifts reflect a redistribution of red and green in the plasma membrane rather than a change of intracellular GFP.

Midchannel proteolysis is distinct from the well-studied C-terminal proteolysis (Brawley and Hosey, 1992; De Jongh et al., 1991, 1994; Gao et al., 2001; Gerhardstein et al., 2000; Hell et al., 1993; Hulme et al., 2005, 2006; Lai et al., 1990) in cleavage sites and consequences: the core of $Ca_v1.2$ remains intact after C-terminal proteolysis but is split following midchannel proteolysis. Our biochemical and imaging experiments both suggest that midchannel proteolysis takes place at several locations of $Ca_v1.2$ (Figures 1D, 1E, 2A, and 2F). As a result, $Ca_v1.2$ channels on the plasma membrane of native cells may be heterogeneous, with some being full-length $Ca_v1.2$ subunits and some being $Ca_v1.2$ fragments of various lengths. Our results from recombinant fragment channels show that they display biophysical properties distinct from full-length channels (Figures 6C–6E). Furthermore, our results show that cleaved $Ca_v1.2$ fragments can dissociate from one another (Figures 2B, 2C, and 2F), and while these fragments do not form functional channels on their own (Figure 6B), some of them can alter the biophysical properties of full-length channels (Figures 6F–6L). Thus, $Ca_v1.2$ currents in native cells could be produced by a highly heterogeneous population of channels. How fragment channels change full-length $Ca_v1.2$ properties is unclear; possibilities include competition for the ancillary subunits (β and/or $\alpha_2\delta$) or a direct association with $Ca_v1.2$.

VGCCs are regulated by a host of Ca^{2+}-binding proteins and undergo Ca^{2+}-dependent inactivation (CDI) involving calmodulin (Christel and Lee, 2012). Why do neurons need yet another Ca^{2+}-dependent negative-feedback mechanism, and one as drastic as midchannel proteolysis? For neuroprotection, it is not surprising if neurons utilize multiple or even redundant means to diligently control the activity of channels as essential as VGCCs. There may also be significant differences between CDI and midchannel proteolysis for neurons to exploit. For example, CDI can occur quickly to affect VGCC activity within milliseconds (Tadross et al., 2008; Christel and Lee, 2012); midchannel proteolysis, on the other hand, takes longer and may affect not only VGCC activity but also intracellular Ca^{2+} homeostasis. Furthermore, while CDI mainly assists VGCC inactivation, the consequences of midchannel proteolysis can involve Ca^{2+} current attenuation, channel biophysical property changes, and perhaps putative nonchannel functions of the nascent fragments.

It has been shown that $Ca_v1.2$ and $Ca_v2.2$ undergo ubiquitination and proteasomal degradation, and that these events are regulated by $Ca_v\beta$ (Altier et al., 2011; Waithe et al., 2011). In the absence of $Ca_v\beta$, $Ca_v1.2$ is robustly ubiquitinated and is targeted to the proteasome for degradation; association of $Ca_v\beta$ attenuates $Ca_v1.2$ ubiquitination and prevents endoplasmic reticulum (ER)-associated protein degradation (ERAD), leading to an increased surface expression of $Ca_v1.2$ (Altier et al., 2011). It is unclear whether and how midchannel proteolysis relates to ERAD, but imaging experiments revealed that separation of proteolytically cleaved $Ca_v1.2$ fragments was unaltered by the overexpression of $\alpha_2\delta$ and β subunits (Figures S2C and S2D), suggesting that either these auxiliary subunits do not affect midchannel proteolysis or that the channels undergoing

midchannel proteolysis already have associated endogenous $\alpha_2\delta$ and $Ca_v\beta$ subunits.

Where does $Ca_v1.2$ midchannel proteolysis take place, on the plasma membrane or in an intracellular compartment? Although our results do not provide a definitive answer, they are consistent with the possibility that midchannel proteolysis occurs on the plasma membrane: (1) cleaved complementary $Ca_v1.2$ fragments are present on the plasma membrane (Figures 1C–1E and 2A); (2) it is not affected by the overexpression of $\alpha_2\delta$ and β subunits (Figures S2C and S2D); (3) it is dependent on the ubiquitin-proteasome system, being greatly reduced by a cocktail of ubiquitination and proteasome inhibitors or when a putative ubiquitination site on $Ca_v1.2$ is mutated (Figures 3C and 3D); and (4) it is significantly reduced (Figure 3F) or virtually abolished (Figure 3G) when PEST sequences in $Ca_v1.2$ are deleted. PEST sequences serve as signals for rapid proteolysis by yet unknown proteases (with calpain as a candidate) or by proteasomal degradation, presumably by recruiting proper proteases to the target protein or directing the target protein to proteasomes (Rechsteiner and Rogers, 1996). It has been reported that the two PEST sequences in $Ca_v1.2$ are involved in Akt-mediated increase of calcium channel currents (Catalucci et al., 2009). Akt is thought to phosphorylate $Ca_v\beta_2$, resulting in the masking of the PEST sequences and, consequently, decreased degradation of surface $Ca_v1.2$. Consistent with this notion, deleting each PEST sequence individually increases the stability and current density of $Ca_v1.2$ channels expressed in COS-7 or tsA-201 cells (Catalucci et al., 2009). The precise role of the two PEST sequences and why PEST1 is more effective than PEST3 in aiding $Ca_v1.2$ midchannel proteolysis remain to be investigated. These sequences are probably not the cleavage sites themselves. We speculate that PEST1, because of its location and/or conformation in the three-dimensional structure of $Ca_v1.2$, is more effective than PEST3 in recruiting calpain to $Ca_v1.2$.

Many other questions remain to be elucidated, including the kinetics of midchannel proteolysis, additional proteases involved, precise cleavage sites in $Ca_v\alpha_1$, and the fate and function of the resulting fragment channels. It will be interesting to examine whether other types of VGCCs and other multirepeat ion channels such as Na^+ channels also undergo midchannel proteolysis. Truncated forms of $Ca_v\alpha_1$, generated by either alternative splicing or disease-causing mutations, are naturally present in muscles and neurons (Jeng et al., 2008; Malouf et al., 1992; Mezghrani et al., 2008; Okagaki et al., 2001; Page et al., 2004; Pietrobon, 2010; Scott et al., 1998; Wappl et al., 2002). The fragment channels produced by regulated midchannel proteolysis, as well as these short forms of $Ca_v\alpha_1$, may play important roles in both physiological and pathological conditions.

EXPERIMENTAL PROCEDURES

Constructs

Rat (*Rattus norvegicus*) brain $Ca_v1.2$ was used for transfection in hippocampal neurons. GFP was linked to the N terminus of $Ca_v1.2$ to generate LGN. HA epitopes were cloned on LGN at different extracellular locations to generate GFP- and HA-tagged LGH1, LGH2, and LGH3, in which the HA tag was placed, respectively, between residues T320 and G321, Q683 and T684, and G1136 and P1137. A proteolytic motif (ENLYFQG) for TEVp was introduced on LGH3 between II-III loop residues D815 and G816 (LGH3_TEVp). On LGH3_PY/AA, P1364 and Y1365 were each mutated to alanine. Residues 840–861 and 446–459 were deleted to generate LGH3_ΔPEST3 and LGH3_ΔPEST1, respectively. $Ca_v1.2$ fragment channels were engineered to encompass the following channel regions: A1: M1–D449, A2: E450–L2143; B1: M1–S866, B2: M867–L2143; C1: M1–W1216, C2: Y1217–L2143. For oocyte macropatch recordings, rabbit $Ca_v2.1$ was used. $Ca_v2.1$_TEVp carried the TEVp cutting motif at three different locations: G419-A420 (loop I-II), L1096-S1097, and G1218-P1219 (loop II-III).

Cortical Slice Surface Protein Biotinylation

Neocortical slices (400 μm thick, cut horizontally) were obtained from 6-week-old male rat brain and were incubated at 35°C–37°C in oxygenated artificial cerebrospinal fluid (ACF; 119 mM NaCl, 26 mM $NaHCO_3$, 1.25 mM NaH_2PO_4, 2.5 mM KCl, 15 mM glucose, 1 mM myo-inositol, 2 mM pyruvate, 0.4 mM ascorbic acid) for 20–60 min before any pharmacological treatments. For biotinylation of surface proteins, slices were rapidly collected in ice-cold bubbled ACF containing 1 mg/ml sulfo-NHS-SS-biotin (Pierce) for 45 min. Quenching solution was added for 5 min. Solubilization, incubation with neutravidin-agarose beads, washing, and elution of surface proteins for SDS-PAGE and western blot were performed according to Pierce's instructions, with modifications for neocortical slices described in detail in Supplemental Experimental Procedures.

All experiments involving vertebrate animals were performed in accordance with Columbia University's Institute of Comparative Medicine and Institutional Animal Care and Use Committee regulations.

Cortical Slice Age Comparison

For the aging study of Figure 7A, the procedure described above was upgraded to handle four or more animals of different ages in strict parallel, as described in detail in Supplemental Experimental Procedures.

Verapamil Feeding of Aged Animals

Verapamil was used to medicate the drinking water of aged rats, at 12.5 mg/day, for 3–5 weeks. Dosage calculation and details of verapamil administration are explained in Supplemental Experimental Procedures.

Hippocampal Neuron Culture, Transfection, and Surface Biotinylation

Embryonic hippocampi were isolated and primary cultures were grown using standard procedures (Blanpied et al., 2002). Twenty-four hours after plating and then every 4 days, neurobasal medium containing B-27 and l-glutamax (Invitrogen) was used to replace 50% of the culture medium. Neurons were kept at 37°C in a 5% CO_2 humid atmosphere. Hippocampal neurons 10–13 days in vitro were transfected with an optimized method using Lipofectamine 2000 (Invitrogen). DNA (1.5 μg) in 100 μl Opti-MEM (Invitrogen) was used to transfect each 12 mm diameter coverslip. Surface biotinylation was similar to that described for cortical slices.

Hippocampal Neuron Immunofluorescence and Imaging

Hippocampal neurons were fixed with 2% paraformaldehyde and immunostained 24–48 hr posttransfection. To visualize surface HA tags, neurons were incubated with a mouse monoclonal anti-HA (Covance) for 1 hr in PBS containing 0.5% fish gelatin and 10% goat serum, and then washed with PBS four times. The goat anti-mouse secondary antibody conjugated to the Alexa 594 fluorophore (Invitrogen) was added to the neurons for 1 hr in the same buffer composition. The stained coverslips were washed and mounted on imaging slides using an antifade reagent (Biomeda). All procedures were done at room temperature.

Confocal imaging was performed using a spinning disc microscope. Optical slice thickness was 300 nm. Confocal images for each fluorophore in multilabeling experiments were acquired separately (sequential scans). Images were analyzed using Volocity (PerkinElmer) and MATLAB (MathWorks).

Imaging Data Quantification and Histogram Construction

A software routine was created to scan optical sections of dendrites and automatically select the red objects, which presumably represent surface $Ca_v1.2$. These objects vary in size and are divided into a volume unit called the voxel,

which has a dimension of 0.211 × 0.211 × 0.211 μm and a volume of 0.00944 μm^3. Typically, ~10,000–15,000 voxels were generated for each neuron. The red and green intensity was measured for each voxel and the red/green ratio (i.e., NCI) was determined. The NCI of all the voxels was binned and plotted in a frequency (ordinate, y axis) versus NCI (abscissa, x axis) graph. This resulting distribution (curve) shows the percentage of voxels that exhibit the NCI above a threshold value.

In ensemble % frequency above threshold versus NCI curves using data pooled from multiple neurons, the x axis consisted of step thresholds used to bin the entire population of NCI values. Typically, a group of ~15 neurons produced ~150,000–200,000 voxels. x axis thresholds were a sequence of logarithmically spaced numbers generated by MATLAB to represent values between 0.1 and 10 (listed in Supplemental Experimental Procedures). y axis data points from all the neurons in any given group were averaged and plotted.

Xenopus Oocyte Preparation, Injection, and Surface Biotinylation

Female oocyte-positive *Xenopus laevis* (African clawed) frogs were purchased from *Xenopus* I, *Xenopus* Express, or Nasco, and stage V-VI oocytes were isolated. Briefly, frogs were anesthetized in a 0.3% tricaine solution. Ovarian lobes were excised in OR2 (Ca^{2+}-free) solution (82.4 mM NaCl, 2.5 mM KCl, 1 mM $MgCl_2$, 5 mM HEPES) and digested in OR2 supplemented with collagenase A (0.2–0.5 mg/ml; Roche) for 2–3 hr at room temperature. Oocytes were washed and recovered in ND96 solution (96 mM NaCl, 2.5 mM KCl, 1 mM $MgCl_2$, 5 mM HEPES, 1.8 mM $CaCl_2$, supplemented with penicillin/streptomycin). mRNA injection and oocyte surface biotinylation protocols are presented in detail in Supplemental Experimental Procedures.

Electrophysiology

For whole-cell recording of hippocampal neurons, the pipette solution contained 122 mM CsCl, 10 mM HEPES, 10 mM EGTA, 5 mM $MgCl_2$, 4 mM MgATP, and 0.4 mM GTP (pH 7.2 adjusted with CsOH). Recording electrodes had resistances of 2–4 MΩ. The bath solution contained 115 mM NaCl, 20 mM tetraethylammonium hydroxide, 5 mM KCl, 2 mM $MgCl_2$, 5 mM $BaCl_2$, 10 mM HEPES, and 10 mM D-glucose (pH 7.4 adjusted with NaOH). Tetradotoxin (1 μM) was added before recordings.

For two-electrode voltage-clamp recordings of oocytes, the bath solution contained 10 mM $BaCl_2$, 5 mM KCl, 60 mM tetraethylammonium hydroxide, 20 mM NaOH, and 5 mM HEPES (pH 7.4 adjusted with methanesulfonic acid).

For inside-out macropatch recordings from oocytes, $Ca_v2.1$ (P/Q-type) channels were used because of their slower rundown (Zhen et al., 2006). Electrodes had a diameter of 15–30 μm and a resistance of 0.2–0.4 MΩ when filled with a solution containing 45 mM $BaCl_2$, 80 mM KCl, and 10 mM HEPES (pH 7.3 adjusted with KOH). The bath solution contained 125 mM CsCl, 4 mM NaCl, 10 mM HEPES, 10 mM EGTA (pH 7.3 adjusted with KOH). The purified WT or mutant TEV proteases were perfused in the bath solution for 2 min, followed by 1 min of wash.

Data were analyzed with Clampfit (Molecular Devices). All experiments were performed at 22°C–23°C.

Western Immunoblotting

Protein samples were run on 8% acrylamide (Bio-Rad) gels or 4%–12% precast gradient gels (Invitrogen). Electrical transfer to polyvinylidene fluoride (PVDF) membranes (Bio-Rad) was performed in a standard 25 mM Tris, 192 mM glycine (pH ~8.3) buffer supplemented with 0.002% SDS for 90 min at 90 V at 4°C. Membranes were handled in PBS containing 0.2% Tween 20 (PBST). Blocking buffer was 10% newborn calf serum (GIBCO) plus 1% fish gelatin (Sigma) in PBST. Primary antibodies were used at 1:750–1:1,000 dilutions, and were purchased from Sigma (anti-L_{II-III} and anti-Nt), Cell Signaling (anti-PARP), and Abcam (anti-Na^+/K^+ ATPase). Anti-Ct, generated against residues 2155–2171 of rabbit cardiac $Ca_v1.2$ (Hulme et al., 2006), was a courteous gift from W.A. Catterall and R. Westenbroek. Secondary antibody (goat anti-rabbit, horseradish peroxidase-conjugated; Santa Cruz Biotechnology) was used at 1:2,000 dilution. Protein bands were visualized using enhanced chemiluminescence reagents (Pierce) on X-ray film (Kodak). For stripping and reprobing of PVDF membranes, the stripping buffer contained 100 mM β-mercaptoethanol, 2% SDS, and 62.5 mM Tris•HCl (pH 6.8). Coomassie blue staining was performed using Biosafe Coomassie (Bio-Rad) according to the manufacturer's instructions or using a stain consisting of 0.1% Coomassie brilliant blue R-250 in 40% MeOH and 1% acetic acid.

Purification of Tobacco Etch Virus Protease

For protein synthesis in *Escherichia coli*, DE3 bacteria were used for cDNA transformation and protein expression. The expressed recombinant tobacco etch virus protease (Addgene plasmid 8827: pRK793) construct contained a maltose-binding protein (MBP) molecule for enhanced expression, a TEVp self-cleavage recognition site (ENLYFQG), a His tag, and finally TEVp itself. Ultimately, TEVp was isolated from transformed DE3 bacteria using a nickel-bead column system as described in Supplemental Experimental Procedures. Western blot with an antibody against TEVp (courtesy of Michael Ehrmann) revealed that the purified TEVp had the expected molecular mass of TEVp plus the His tag (27 kDa), indicating that the tagged MBP molecule had been removed from the parent construct by TEVp self-cleavage (Figure S6A). In contrast, the molecular mass of the purified C151A mutant protease was significantly higher (70 kDa) than that of WT TEVp (Figure S6A), as expected for the original MBP-tagged parent construct, confirming the loss of catalytic activity caused by the C151A mutation.

Statistics

Data are represented as mean ± SEM and asterisks denote statistical differences throughout. For all statistical tests used and their resulting p values, see Supplemental Experimental Procedures.

SUPPLEMENTAL INFORMATION

Supplemental Information includes Supplemental Experimental Procedures and seven figures and can be found with this article online at http://dx.doi.org/10.1016/j.neuron.2014.04.017.

ACKNOWLEDGMENTS

We thank Drs. William Catterall and Ruth Westenbroek of the University of Washington for the anti-Ct antibody, Dr. Michael Ehrmann of the University of Duisburg-Essen for the anti-TEVp antibody, Glynis Gordon and Rachel Schenkel for technical assistance, and Dr. Zafir Buraei of Pace University and members of the J.Y. laboratory for commenting on the manuscript. This work was supported by National Institutes of Health grants NS053494 and NS045383 (to J.Y.), an Established Investigator Award of the American Heart Association (to J.Y.), the Top Talents Program of Yunnan Province, China (to J.Y.), and a postdoctoral fellowship (0625908T) from the American Heart Association (to I.E.M.). M.D.E. is an employee and shareholder of Pfizer.

Accepted: April 1, 2014
Published: June 4, 2014

REFERENCES

Altier, C., Garcia-Caballero, A., Simms, B., You, H., Chen, L., Walcher, J., Tedford, H.W., Hermosilla, T., and Zamponi, G.W. (2011). The $Ca_v\beta$ subunit prevents RFP2-mediated ubiquitination and proteasomal degradation of L-type channels. Nat. Neurosci. *14*, 173–180.

Blanpied, T.A., Scott, D.B., and Ehlers, M.D. (2002). Dynamics and regulation of clathrin coats at specialized endocytic zones of dendrites and spines. Neuron *36*, 435–449.

Brawley, R.M., and Hosey, M.M. (1992). Identification of two distinct proteins that are immunologically related to the α_1 subunit of the skeletal muscle dihydropyridine-sensitive calcium channel. J. Biol. Chem. *267*, 18218–18223.

Cain, S.M., and Snutch, T.P. (2011). Voltage-gated calcium channels and disease. Biofactors *37*, 197–205.

Catalucci, D., Zhang, D.H., DeSantiago, J., Aimond, F., Barbara, G., Chemin, J., Bonci, D., Picht, E., Rusconi, F., Dalton, N.D., et al. (2009). Akt regulates L-type Ca^{2+} channel activity by modulating $Ca_v\alpha1$ protein stability. J. Cell Biol. *184*, 923–933.

Catterall, W.A. (2000). Structure and regulation of voltage-gated Ca^{2+} channels. Annu. Rev. Cell Dev. Biol. *16*, 521–555.

Chaitanya, G.V., Steven, A.J., and Babu, P.P. (2010). PARP-1 cleavage fragments: signatures of cell-death proteases in neurodegeneration. Cell Commun. Signal. *8*, 31.

Christel, C., and Lee, A. (2012). Ca^{2+}-dependent modulation of voltage-gated Ca^{2+} channels. Biochim. Biophys. Acta *1820*, 1243–1252.

Deisseroth, K., Mermelstein, P.G., Xia, H., and Tsien, R.W. (2003). Signaling from synapse to nucleus: the logic behind the mechanisms. Curr. Opin. Neurobiol. *13*, 354–365.

De Jongh, K.S., Warner, C., Colvin, A.A., and Catterall, W.A. (1991). Characterization of the two size forms of the α_1 subunit of skeletal muscle L-type calcium channels. Proc. Natl. Acad. Sci. USA *88*, 10778–10782.

De Jongh, K.S., Colvin, A.A., Wang, K.K., and Catterall, W.A. (1994). Differential proteolysis of the full-length form of the L-type calcium channel α_1 subunit by calpain. J. Neurochem. *63*, 1558–1564.

Di Biase, V., Tuluc, P., Campiglio, M., Obermair, G.J., Heine, M., and Flucher, B.E. (2011). Surface traffic of dendritic $Ca_V1.2$ calcium channels in hippocampal neurons. J. Neurosci. *31*, 13682–13694.

Dolmetsch, R. (2003). Excitation-transcription coupling: signaling by ion channels to the nucleus. Sci. STKE *2003*, PE4.

Ebihara, T., Komiya, Y., Izumi-Nakaseko, H., Adachi-Akahane, S., Okabe, S., and Okamura, Y. (2002). Coexpression of a Ca(v)1.2 protein lacking an N-terminus and the first domain specifically suppresses L-type calcium channel activity. FEBS Lett. *529*, 203–207.

Fuller, M.D., Emrick, M.A., Sadilek, M., Scheuer, T., and Catterall, W.A. (2010). Molecular mechanism of calcium channel regulation in the fight-or-flight response. Sci. Signal. *3*, ra70.

Gao, T., Cuadra, A.E., Ma, H., Bunemann, M., Gerhardstein, B.L., Cheng, T., Eick, R.T., and Hosey, M.M. (2001). C-terminal fragments of the α1C ($Ca_V1.2$) subunit associate with and regulate L-type calcium channels containing C-terminal-truncated α1C subunits. J. Biol. Chem. *276*, 21089–21097.

Gerhardstein, B.L., Gao, T., Bünemann, M., Puri, T.S., Adair, A., Ma, H., and Hosey, M.M. (2000). Proteolytic processing of the C terminus of the α(1C) subunit of L-type calcium channels and the role of a proline-rich domain in membrane tethering of proteolytic fragments. J. Biol. Chem. *275*, 8556–8563.

Hell, J.W., Yokoyama, C.T., Wong, S.T., Warner, C., Snutch, T.P., and Catterall, W.A. (1993). Differential phosphorylation of two size forms of the neuronal class C L-type calcium channel α1 subunit. J. Biol. Chem. *268*, 19451–19457.

Hell, J.W., Westenbroek, R.E., Breeze, L.J., Wang, K.K., Chavkin, C., and Catterall, W.A. (1996). *N*-methyl-D-aspartate receptor-induced proteolytic conversion of postsynaptic class C L-type calcium channels in hippocampal neurons. Proc. Natl. Acad. Sci. USA *93*, 3362–3367.

Hulme, J.T., Konoki, K., Lin, T.W., Gritsenko, M.A., Camp, D.G., II, Bigelow, D.J., and Catterall, W.A. (2005). Sites of proteolytic processing and noncovalent association of the distal C-terminal domain of $Ca_V1.1$ channels in skeletal muscle. Proc. Natl. Acad. Sci. USA *102*, 5274–5279.

Hulme, J.T., Yarov-Yarovoy, V., Lin, T.W., Scheuer, T., and Catterall, W.A. (2006). Autoinhibitory control of the $Ca_V1.2$ channel by its proteolytically processed distal C-terminal domain. J. Physiol. *576*, 87–102.

Jeng, C.J., Sun, M.C., Chen, Y.W., and Tang, C.Y. (2008). Dominant-negative effects of episodic ataxia type 2 mutations involve disruption of membrane trafficking of human P/Q-type Ca^{2+} channels. J. Cell. Physiol. *214*, 422–433.

Kordasiewicz, H.B., Thompson, R.M., Clark, H.B., and Gomez, C.M. (2006). C-termini of P/Q-type Ca^{2+} channel α1A subunits translocate to nuclei and promote polyglutamine-mediated toxicity. Hum. Mol. Genet. *15*, 1587–1599.

Lai, Y., Seagar, M.J., Takahashi, M., and Catterall, W.A. (1990). Cyclic AMP-dependent phosphorylation of two size forms of α1 subunits of L-type calcium channels in rat skeletal muscle cells. J. Biol. Chem. *265*, 20839–20848.

Leenders, A.G., van den Maagdenberg, A.M., Lopes da Silva, F.H., Sheng, Z.H., Molenaar, P.C., and Ghijsen, W.E. (2002). Neurotransmitter release from tottering mice nerve terminals with reduced expression of mutated P- and Q-type Ca^{2+}-channels. Eur. J. Neurosci. *15*, 13–18.

Leenders, A.G., Lin, L., Huang, L.D., Gerwin, C., Lu, P.H., and Sheng, Z.H. (2008). The role of MAP1A light chain 2 in synaptic surface retention of $Ca_v2.2$ channels in hippocampal neurons. J. Neurosci. *28*, 11333–11346.

Liao, P., and Soong, T.W. (2010). $Ca_V1.2$ channelopathies: from arrhythmias to autism, bipolar disorder, and immunodeficiency. Pflugers Arch. *460*, 353–359.

Malouf, N.N., McMahon, D.K., Hainsworth, C.N., and Kay, B.K. (1992). A two-motif isoform of the major calcium channel subunit in skeletal muscle. Neuron *8*, 899–906.

Mezghrani, A., Monteil, A., Watschinger, K., Sinnegger-Brauns, M.J., Barrère, C., Bourinet, E., Nargeot, J., Striessnig, J., and Lory, P. (2008). A destructive interaction mechanism accounts for dominant-negative effects of misfolded mutants of voltage-gated calcium channels. J. Neurosci. *28*, 4501–4511.

Moyer, J.R., Jr., Thompson, L.T., Black, J.P., and Disterhoft, J.F. (1992). Nimodipine increases excitability of rabbit CA1 pyramidal neurons in an age- and concentration-dependent manner. J. Neurophysiol. *68*, 2100–2109.

Okagaki, R., Izumi, H., Okada, T., Nagahora, H., Nakajo, K., and Okamura, Y. (2001). The maternal transcript for truncated voltage-dependent Ca^{2+} channels in the ascidian embryo: a potential suppressive role in Ca^{2+} channel expression. Dev. Biol. *230*, 258–277.

Page, K.M., Heblich, F., Davies, A., Butcher, A.J., Leroy, J., Bertaso, F., Pratt, W.S., and Dolphin, A.C. (2004). Dominant-negative calcium channel suppression by truncated constructs involves a kinase implicated in the unfolded protein response. J. Neurosci. *24*, 5400–5409.

Page, K.M., Heblich, F., Margas, W., Pratt, W.S., Nieto-Rostro, M., Chaggar, K., Sandhu, K., Davies, A., and Dolphin, A.C. (2010). N terminus is key to the dominant negative suppression of Ca_V2 calcium channels: implications for episodic ataxia type 2. J. Biol. Chem. *285*, 835–844.

Pietrobon, D. (2010). $Ca_V2.1$ channelopathies. Pflugers Arch. *460*, 375–393.

Raghib, A., Bertaso, F., Davies, A., Page, K.M., Meir, A., Bogdanov, Y., and Dolphin, A.C. (2001). Dominant-negative synthesis suppression of voltage-gated calcium channel $Ca_v2.2$ induced by truncated constructs. J. Neurosci. *21*, 8495–8504.

Raike, R.S., Kordasiewicz, H.B., Thompson, R.M., and Gomez, C.M. (2007). Dominant-negative suppression of $Ca_v2.1$ currents by $\alpha_1$2.1 truncations requires the conserved interaction domain for β subunits. Mol. Cell. Neurosci. *34*, 168–177.

Ramakrishnan, N.A., Drescher, M.J., Sheikhali, S.A., Khan, K.M., Hatfield, J.S., Dickson, M.J., and Drescher, D.G. (2006). Molecular identification of an N-type Ca^{2+} channel in saccular hair cells. Neuroscience *139*, 1417–1434.

Rechsteiner, M., and Rogers, S.W. (1996). PEST sequences and regulation by proteolysis. Trends Biochem. Sci. *21*, 267–271.

Sakurai, T., Hell, J.W., Woppmann, A., Miljanich, G.P., and Catterall, W.A. (1995). Immunochemical identification and differential phosphorylation of alternatively spliced forms of the α1A subunit of brain calcium channels. J. Biol. Chem. *270*, 21234–21242.

Schiff, M.L., Siderovski, D.P., Jordan, J.D., Brothers, G., Snow, B., De Vries, L., Ortiz, D.F., and Diversé-Pierluissi, M. (2000). Tyrosine-kinase-dependent recruitment of RGS12 to the N-type calcium channel. Nature *408*, 723–727.

Scott, V.E., Felix, R., Arikkath, J., and Campbell, K.P. (1998). Evidence for a 95 kDa short form of the α1A subunit associated with the ω-conotoxin MVIIC receptor of the P/Q-type Ca^{2+} channels. J. Neurosci. *18*, 641–647.

Smoller, J.W., Craddock, N., Kendler, K., Lee, P.H., Neale, B.M., Nurnberger, J.I., Ripke, S., Santangelo, S., and Sullivan, P.F.; Cross-Disorder Group of the Psychiatric Genomics Consortium; Genetic Risk Outcome of Psychosis (GROUP) Consortium (2013). Identification of risk loci with shared effects on five major psychiatric disorders: a genome-wide analysis. Lancet *381*, 1371–1379.

Striessnig, J., Bolz, H.J., and Koschak, A. (2010). Channelopathies in $Ca_v1.1$, $Ca_v1.3$, and $Ca_v1.4$ voltage-gated L-type Ca^{2+} channels. Pflugers Arch. *460*, 361–374.

Tadross, M.R., Dick, I.E., and Yue, D.T. (2008). Mechanism of local and global Ca^{2+} sensing by calmodulin in complex with a Ca^{2+} channel. Cell *133*, 1228–1240.

Thibault, O., and Landfield, P.W. (1996). Increase in single L-type calcium channels in hippocampal neurons during aging. Science *272*, 1017–1020.

Thibault, O., Porter, N.M., Chen, K.C., Blalock, E.M., Kaminker, P.G., Clodfelter, G.V., Brewer, L.D., and Landfield, P.W. (1998). Calcium dysregulation in neuronal aging and Alzheimer's disease: history and new directions. Cell Calcium *24*, 417–433.

Waithe, D., Ferron, L., Page, K.M., Chaggar, K., and Dolphin, A.C. (2011). β-subunits promote the expression of $Ca_V2.2$ channels by reducing their proteasomal degradation. J. Biol. Chem. *286*, 9598–9611.

Wappl, E., Koschak, A., Poteser, M., Sinnegger, M.J., Walter, D., Eberhart, A., Groschner, K., Glossmann, H., Kraus, R.L., Grabner, M., and Striessnig, J. (2002). Functional consequences of P/Q-type Ca^{2+} channel $Ca_v2.1$ missense mutations associated with episodic ataxia type 2 and progressive ataxia. J. Biol. Chem. *277*, 6960–6966.

Westenbroek, R.E., Sakurai, T., Elliott, E.M., Hell, J.W., Starr, T.V., Snutch, T.P., and Catterall, W.A. (1995). Immunochemical identification and subcellular distribution of the α1A subunits of brain calcium channels. J. Neurosci. *15*, 6403–6418.

Wheeler, D.G., Groth, R.D., Ma, H., Barrett, C.F., Owen, S.F., Safa, P., and Tsien, R.W. (2012). Ca(V)1 and Ca(V)2 channels engage distinct modes of Ca(2+) signaling to control CREB-dependent gene expression. Cell *149*, 1112–1124.

Woppmann, A., Ramachandran, J., and Miljanich, G.P. (1994). Calcium channel subtypes in rat brain: biochemical characterization of the high-affinity receptors for ω-conopeptides SNX-230 (synthetic MVIIC), SNX-183 (SVIB), and SNX-111 (MVIIA). Mol. Cell. Neurosci. *5*, 350–357.

Zamponi, G.W., and Currie, K.P. (2013). Regulation of Ca(V)2 calcium channels by G protein coupled receptors. Biochim. Biophys. Acta *1828*, 1629–1643.

Zamponi, G.W., Lory, P., and Perez-Reyes, E. (2010). Role of voltage-gated calcium channels in epilepsy. Pflugers Arch. *460*, 395–403.

Zhen, X.G., Xie, C., Yamada, Y., Zhang, Y., Doyle, C., and Yang, J. (2006). A single amino acid mutation attenuates rundown of voltage-gated calcium channels. FEBS Lett. *580*, 5733–5738.